Local transport measurements in graphene on SiO_2 using Kelvin probe force microscopy

Philip Willke [a], Christian Möhle [a], Anna Sinterhauf [a], Thomas Kotzott [a], Hak Ki Yu [b, c, d], Alec Wodtke [b, c], Martin Wenderoth [a, *]

[a] IV. Physical Institute, University of Göttingen, 37077, Göttingen, Germany
[b] Institute for Physical Chemistry, University of Göttingen, 37077, Göttingen, Germany
[c] Max Planck Institute for Biophysical Chemistry, 37077, Göttingen, Germany
[d] Department of Materials Science & Engineering, Ajou University, Suwon, 443-749, South Korea

ARTICLE INFO

ABSTRACT

By using Kelvin Probe Force Microscopy with an additional applied electric field we investigate the local voltage drop in graphene on SiO_2 under ambient conditions. We are able to quantify the variation of the local sheet resistance and to resolve localized voltage drops at line defects. Our data demonstrates that the resistance of line defects has been overestimated so far. Moreover, we show that wrinkles have the largest resistance, $\rho_{Wrinkle} < 80$ $\Omega\mu m$. Temperature-dependent measurements show that the local monolayer sheet resistance reflects the macroscopic increase in resistance with temperature while the defect resistance for folded wrinkles is best described by a temperature-independent model which we attribute to interlayer tunneling.

1. Introduction

Due to its fascinating electronic structure, graphene is a promising candidate for future device physics including gas sensors, flexible displays and microelectronics [1,2]. Graphene growth by chemical vapor deposition (CVD) and subsequent transfer to SiO_2 has become a favored method for large-scale synthesis [3—5]. During the growth and transfer process structural defects such as wrinkles, grain boundaries and multilayer areas are formed. They can limit the performance of potential devices since they contribute to the resistance and to the heat generation of the sample [6—12].

In contrast to conventional transport measurements, scanning probe techniques can reveal local voltage drops reflecting enhanced resistance associated with features of a sample's microscopic structure; this is a significant advantage. The transport physics of atomic scale defects in graphene on SiC [7,13—15] and SiO_2 [7] has been elucidated by scanning tunneling potentiometry (STP) for low temperatures (6—77 K) and under ultra-high vacuum (UHV) conditions and been analyzed theoretically [16,17]. In contrast, at room temperature and under environmental conditions increased

phonon-scattering dominates the graphene sheet resistance [18] while phase coherent transport processes vanish [9,19].

Using an atomic force microscope (AFM) the method of Kelvin probe force microscopy (KPFM) has been used to map the electrostatic potential in graphene [20—22], functionalized and chemically derived graphene [23,24] and other systems [25,26]. Thus, AFM techniques working under ambient conditions and room temperature are a versatile tool for analyzing the microscopic transport properties in graphene under conditions relevant for device physics.

For graphene, the KPFM technique has been limited so far to the contactless analysis of the local sheet resistance and to the voltage drop at graphene contacts. In this work we quantify for the first time the resistance of a single line defect in graphene under ambient conditions by KPFM. Being smaller than 80 $\Omega\mu m$, we find that most studies overestimate their influence on the total sample resistance. Moreover, we can map local resistances as a function of temperature by using joule heating in our sample.

2. Results and discussion

2.1. Evaluation of KPFM transport measurements

The experimental setup is sketched in Fig. 1a. A graphene

* Corresponding author.
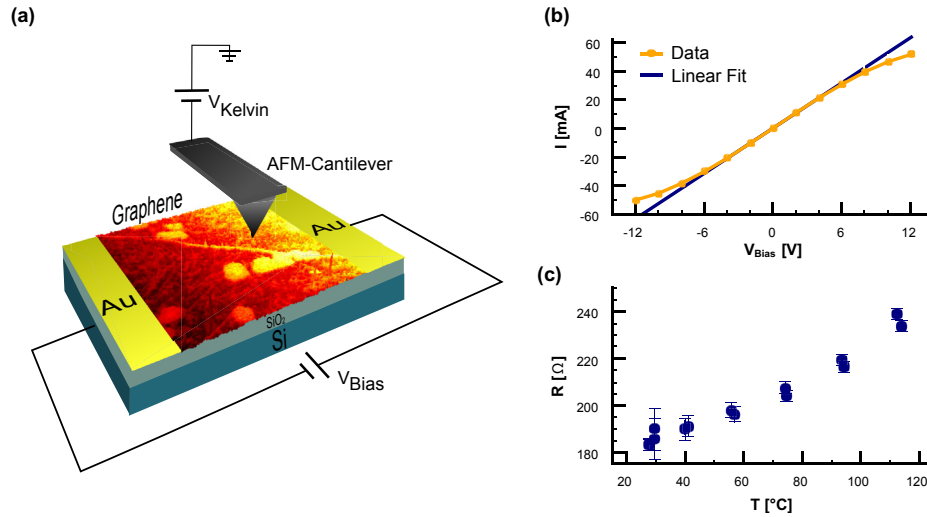 *E-mail address:* mwender@gwdg.de (M. Wenderoth).

Fig. 1. KPFM-setup for local transport measurements. (a) Sketch of the experimental setup. Graphene sample is contacted in two-point geometry allowing to apply V_{Bias} across the sample while $V_{Kelvin}(x,y)$ is measured by the AFM. (b) IV-characteristic of the device. The non-linearity for higher V_{Bias} is induced by the increase in temperature T due to Joule-heating. (c) Absolute device resistance as a function of temperature T derived from the data points in (b). (A color version of this figure can be viewed online.)

sample on SiO_2 is investigated by AFM. Additionally, a potential V_{Bias} is applied via two gold contacts inducing a current across the sample. The IV-characteristic of the device is depicted in Fig. 1b showing an increasing non-linearity outside the interval ± 6 V, since the sample resistance increases due to increased temperature induced by Joule-heating. The extracted macroscopic resistance $R(T) = V/I(V,T)$ is depicted in Fig. 1c, now explicitly as a function of temperature (see methods).

To analyze the behavior of the voltage drop on a microscopic scale (also as a function of temperature) we make use of KPFM. Here, a voltage V_{Kelvin} is applied on the tip side to compensate the electrostatic interaction between tip and sample. In most KPFM experiments no external bias voltage V_{Bias} is applied and the measured quantity V_{Kelvin} is equal to the contact potential difference V_{CPD} leading to

$$V_{Kelvin}(x,y) = V_{CPD}(x,y) = \frac{1}{e}\left[\Phi_{tip} - \Phi_{sample}(x,y)\right] \quad (1)$$

where Φ_{tip} and Φ_{sample} are the work functions of the tip and sample, respectively. The contact potential difference $V_{CPD}(x,y)$ of a 30 μm × 30 μm area is shown in Fig. 2b (topography shown in Fig. 2a). Here, the most striking feature is the work function difference between the mostly monolayer graphene covered surface compared to many small islands of bilayer graphene. While $V_{CPD}(x,y)$ does not yield information about the electron transport, it serves as the reference for no applied current and allows additional insight into the electronic structure of the sample. By applying now the additional external bias voltage V_{Bias} the drop of the electro-static potential is superimposed on V_{CPD}:

$$V_{Kelvin}(x,y) = V_{CPD}(x,y) + V_{Bias}(x,y) \quad (2)$$

This is shown in Fig. 2c and d with an applied external bias of $V_{Bias,+} = +4$ V and $V_{Bias,-} = -4$ V, respectively. Both images already demonstrate an apparent problem for the extraction of transport information: since the variation of $V_{CPD}(x,y)$ is still present in the images, a direct evaluation is difficult. However, under the constraint of symmetric transport ($V_{Bias,+} = -V_{Bias,-}$) the pure transport signal can be obtained by subtraction of opposite applied bias voltages:

$$V_{Transport}(x,y) = \frac{1}{2}\left[V_{Kelvin}^{+}(x,y) - V_{Kelvin}^{-}(x,y)\right] \quad (3)$$

with $V_{Kelvin}^{\pm}(x,y) = V_{Kelvin}(x,y,V_{Bias,\pm})$. This effectively cancels the influence of $V_{CPD}(x,y)$ and is shown in Fig. 2e. Now, the voltage drop is dominated by a linear gradient across the whole image. This evaluation method is equivalent to the elimination of thermovolt-age in scanning tunneling potentiometry that we introduced else-where [13] and is similar to our recently reported work where KPFM was applied to evaluate the graphene/gold-contact resis-tance [20]. Yan et al. also subtracted $V_{Kelvin}^{+}(x,y) - V_{Kelvin}^{0V}(x,y)$ [23], which is also valid if the surface potential does not change under the influence of current or temperature. We emphasize that Fig. 2e clearly demonstrates that complete 2D transport maps can be ob-tained with this method. In addition, the contact potential differ-ence $V_{CPD}(x,y)$ can be recovered from the maps in Fig. 2c and d by simple addition.

$$V_{CPD}^{restored}(x,y) = \frac{1}{2}\left[V_{Kelvin}^{+}(x,y) + V_{Kelvin}^{-}(x,y)\right] \quad (4)$$

Comparing Fig. 2f with the original contact potential difference in Fig. 2b, we see that the assumption of symmetric transport is valid [13]. Fig. 2g shows the averaged potential drop across the sample in the x- and y-directions. Clearly, the voltage drop occurs mainly in x-direction and much less (7%) along the y-direction.

Variations in the voltage drop are found on a local scale. We calculated the local sheet resistance $\rho_{ML} = E_{ML}/j_{macro}$ with the electric field on the monolayer areas E_{ML} and the macroscopically measured current density j_{macro} for several areas indicated in Fig. 2e and f. The electric field on the monolayer areas can be calculated by $E_{ML} = \Delta V/\Delta x$, the slope of the voltage drop ΔV over the distance Δx. Besides, the macroscopic current density is defined as $j_{macro} = V_{Bias} \cdot W/R$ with the width W of the sample and the sample resistance R as shown in Fig. 1c. The result can be found together with the macroscopic sheet resistance ρ_{macro} in Fig. 2h. Two ob-servations can be made. First, the local monolayer resistance is $\approx 10\%$ smaller than the macroscopically measured sheet resistance ρ_{macro}. Reasons for this lower value are the observed voltage drop in y-direction which can be introduced by small deviations in the alignment of the sample. Possibly, the contact resistance between
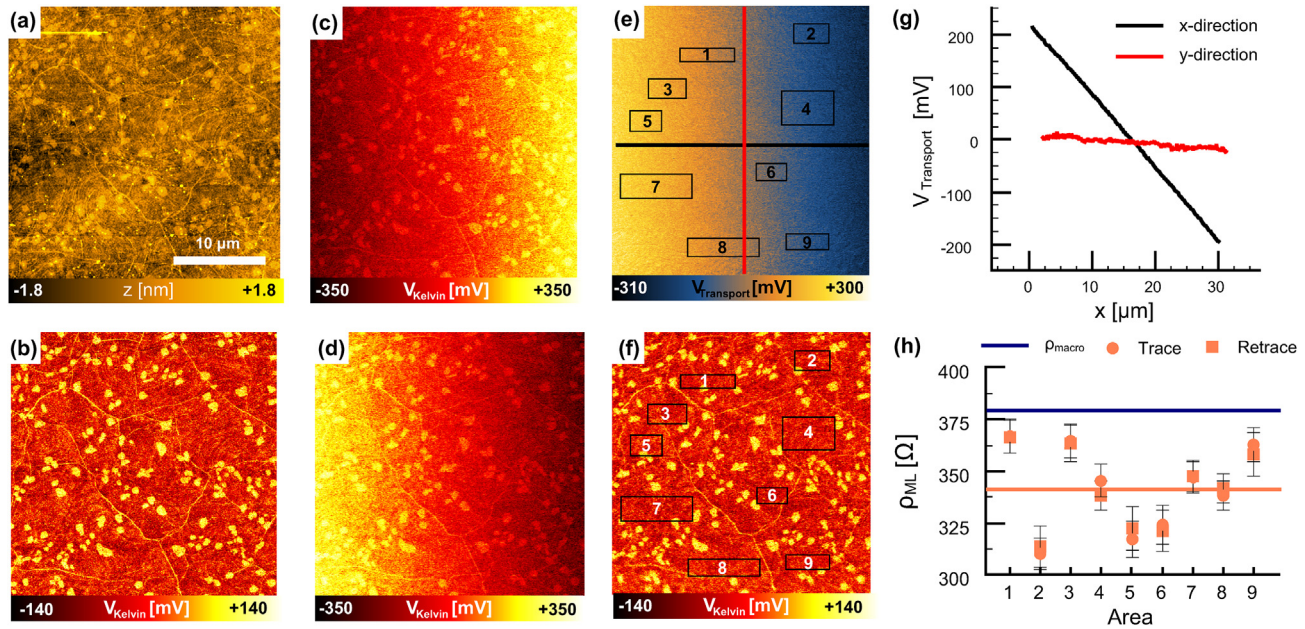
Fig. 2. AFM transport study on a scale of 30 μm × 30 μm (a) topography image of graphene on SiO_2. (b) V_{Kelvin} without applied bias voltage V_{Bias}. (c) V_{Kelvin} for additional applied bias voltage $V_{Bias,+} = +4$ V and (d) $V_{Bias,-} = -4$ V. (e) $V_{Transport}$ evaluated by subtracting the KPFM data in (c) and (d). (f) Addition of (c) and (d) reveals the reconstructed V_{Kelvin}-measurement equivalent to the case of no applied bias voltage in (b). (g) Voltage drop in x-direction (black) and y-direction (red) by averaging over the whole image in (e) along the indicated lines. (h) Local monolayer sheet resistance ρ_{ML} for 9 different areas indicated in (e) and (f). Darkblue line indicates the macroscopic sheet resistance ρ_{macro} while the yellow line is the average of the local measurements ρ_{ML}. (A color version of this figure can be viewed online.)

gold and graphene can contribute to the voltage drop which is however relatively small [20]. In addition, the influence of localized defects as ML/BL-interfaces, steps and wrinkles can give a significant contribution to the total resistance as in the case of graphene on SiC [13,15]. The comparably small difference to ρ_{macro} already limits this influence to ≤ 10%. The second observation is that the monolayer sheet resistance ρ_{ML} varies by up to 8% from the average value $\rho_{ML} = 342$ Ω. Reasons for this can be a different density of defects such as smaller wrinkles present on the sample as well as local differences in doping and differences in coupling to the substrate. Moreover, it has been shown that the size of single graphene grains has an influence on the total resistance [10]. Since grain boundaries are not visible within AFM measurements we cannot evaluate this quantitatively, while the grain size (<10 μm) is clearly smaller than the image size. The evaluation of any local resistance from the voltage drop is only legitimate, if the local current density is sufficiently homogeneous and not locally varying due to e.g. defects. In order to estimate the effects of inhomogeneities in the current density, we have performed resistor network simulations of the system (see Supporting Information). The current is found to be mainly homogeneous (coefficient of variation 3.8%), thus employing the macroscopic quantity j_{macro} is justified and only holds a small error for the values of local resistances.

2.2. Temperature dependence of local resistances

As already discussed for the macroscopic case, the macroscopic resistance ρ_{macro} increases with temperature T due to Joule-heating. In Fig. 3 we demonstrate that this is also true at the microscopic scale. For the two monolayer areas indicated in the topography (Fig. 3a) and the KPFM map (Fig. 3b) we measured the electric field E_{ML} for different bias voltages V_{Bias} in the range between ±4 V and ±12 V. The latter can be expressed as the macroscopic current density j_{macro}. Fig. 3c depicts the electric field E_{ML} as a function of j_{macro} which would be linear if temperature did not vary and for the

Ohmic case. The deviation from linearity reveals the temperature dependence of the resistance. In Fig. 3d we show the calculated temperature dependent sheet resistance for both areas together with that of the macroscopic sample. All show a similar slope. The increase in sheet resistance with temperature for graphene on SiO_2 can be explained by additional contributions from acoustic phonons ($\rho(T) \propto T$) and from the activation process of two surface phonon modes in SiO_2 ($\rho(T) \propto (e^{E_0/k_B T} - 1)^{-1}$) [18]. The fits to the data using this model are shown as lines in Fig. 3d. The macroscopic change and the two microscopic values yield similar values for the activation energy E_0. The variation of the curves in Fig. 3d only stems from the temperature-independent part ρ_0 varying in the range as discussed in Fig. 2h (see Supporting Information). This part is amongst others depending on gate voltage/electron concentration [18]. While no gate voltage has been applied in this experiment, local changes in doping as well as different concentration of atomic scale defects can lead to local variations of this term.

2.3. Resistance of line defects

A variety of line defects, such as grain boundaries, ML/BL-interfaces and wrinkles can be found on our samples; however, they hardly influence the transport compared to e.g. graphene on SiC [13,15]. As demonstrated in Fig. 2e, the main voltage drop is found on the free graphene terraces. Nevertheless, by carefully analyzing the voltage drop in the vicinity of a defect, their small contributions to the resistance can be observed.

One of the most prominent defects are folded graphene wrinkles, one of which can be seen in the middle of Fig. 3a–b (Defect #4). According to Zhu et al. these are formed when a wrinkle's height becomes large enough to result in instability and collapse [11]. It then forms a local quasi-trilayer (TRL) graphene region. Therefore, they are comparably wide yet smaller in height compared to unfolded wrinkles (Fig. 4a left/middle). The folded graphene wrinkles analyzed here are between 150 and 300 nm
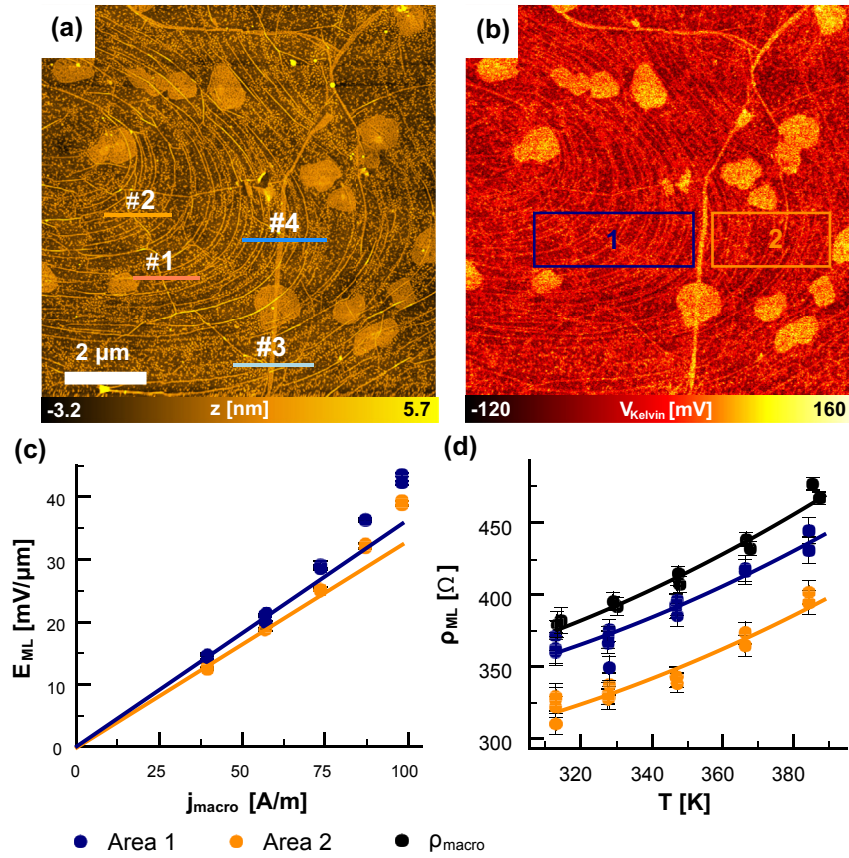
Fig. 3. Temperature-dependence of local sheet resistance ρ_{ML}(T). (a) Topography map and (b) KPFM map without applied bias voltage. (c) Electric field E_{ML} as a function of j_{macro} for the two areas indicated in (b). Lines are fitted to the data points of lowest current density. (d) Local monolayer sheet resistances ρ_{ML}(T) as a function of temperature T calculated from the data in (c). Black points show the macroscopic sheet resistance ρ_{macro}(T) derived from the data in Fig. 1(c) and the device geometry. Lines indicate the fit to the model described in the text. (A color version of this figure can be viewed online.)
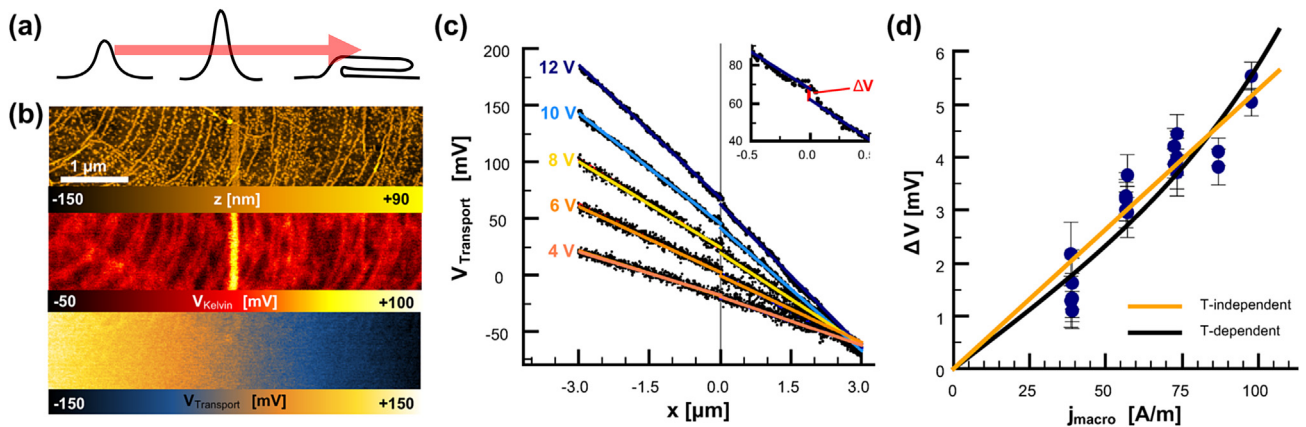

Fig. 4. Voltage drop at a folded graphene wrinkle. (a) Sketch of the formation of a folded graphene wrinkle. In the folded region three layers of graphene are effectively on top of each other. (b) Topography, KPFM and transport map (V_{Bias} = 12 V) for the folded graphene wrinkle in Fig. 3 (#4). (c) Averaged voltage drop $V_{Transport}$ across the data shown in (b) taken for different applied bias voltages V_{Bias}. The x-axis has been adjusted so that the wrinkle is located at x = 0 μm (gray vertical line). Colored lines indicate linear fits to the left and right side of the wrinkle. The inset displays the voltage drop in the vicinity of the wrinkle for V_{Bias} = 12 V with the voltage drop ΔV located at the position of the wrinkle. (d) Voltage drop ΔV for the data in (c) as a function of macroscopic current density j_{macro}. The orange (black) line shows the temperature-independent (temperature-dependent) fit to the data. (A color version of this figure can be viewed online.)

wide and 0.9–1.2 nm in height similar to those reported in [11]. Their anticipated structure can be seen in Fig. 4a according to the model of [11]. In Fig. 4b, we show the topography of the folded wrinkle from the data set in Fig. 3 along with the KPFM and the transport map. The KPFM map clearly shows a strong contrast on the wrinkle indicating its different electronic structure. The work function difference associated with the folded wrinkles $[\Delta\Phi_{Wrinkle-ML} = (85 \pm 5)\,\text{mV}]$ in Fig. 3b is demonstrably higher than that for the bilayer $[\Delta\Phi_{BL-ML} = (71 \pm 5)\,\text{mV}]$. While $\Delta\Phi_{BL-ML}$ is in excellent agreement with other reported values [27], the higher

value for $\Delta\Phi_{Wrinkle - ML}$ is a strong evidence for the TRL-like nature of the folded wrinkle [27]. In Fig. 4c we present averaged sections through the transport map for different applied bias voltages. For a defect resistance $\rho_{Wrinkle}$ we expect a step-like jump in the potential ΔV at the position of the wrinkle (gray line). Note that a defect resistance for a 1D defect is given in $\Omega\mu m$ in contrast to the sheet resistance ρ_{ML} due to its difference in dimension. The jump in potential ΔV can be clearly seen in the inset for $V_{Bias} = 12$ V. For a local scatterer at constant temperature, the size of the potential jump effectively scales with V_{Bias} [15], since

$$\Delta V = \rho_{Wrinkle} \cdot j_{macro}(V_{Bias}) \qquad (5)$$

To evaluate ΔV we fitted straight lines to the voltage drop over the ML sheets to the left and to the right of the wrinkle and determined their difference at the position of the wrinkle as shown in the inset of Fig. 4c. While the evolution of the voltage drop within the defect could give access to further information on the scattering mechanism [13], we cannot exclude crosstalk from V_{Kelvin} (Fig. 4b) that changes significantly on the wrinkle and therefore we do not discuss this further here. In Fig. 4d, we plot ΔV as a function of macroscopic current density j_{macro}. We compare this to predictions of two models of transport: one reflecting the temperature-dependent sheet resistance of the monolayer graphene ρ_{ML} (black line) and one reflecting a temperature-independent voltage drop (orange line). We find that the observations are most consistent with a T-independent transport model (see Supporting Information). This is supported by the results of Grosse et al. who found a large increase in Joule-heating at localized scatterers [12]. Thus, it is possible that the temperature of the folded wrinkles is higher than for the sheet itself. Hence, if $\rho_{Wrinkle}$ were temperature dependent, deviations from the linear behavior of Fig. 4d would be larger than expected. Consequently, we conclude that for the localized scatterer the underlying scattering mechanism shows either a significantly smaller temperature-dependence or is completely independent of temperature.

From the best fit to the data we determine the wrinkle defect resistance, $\rho_{Wrinkle} = (51.9 \pm 2.4)$ $\Omega\mu m$. The lowest reported experimental resistance value for a graphene wrinkle is 200 $\Omega\mu m$ for a 20 nm wide wrinkle [7]. Theoretically, the folded graphene wrinkle was postulated to have a defect resistance 200–300 $\Omega\mu m$ dominated by interlayer tunneling using nonequilibrium Green's function method [11]. Our measurements suggest that the influence of this type of wrinkle has likely been overestimated up to now.

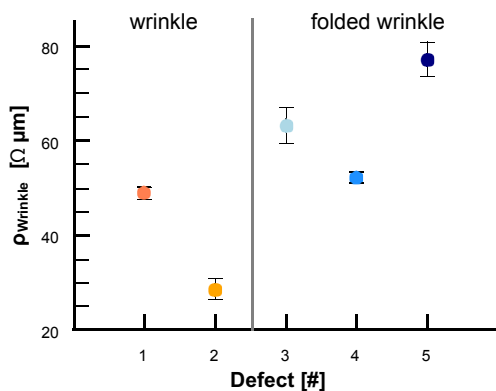In Fig. 5 we show all significant local defects in the area of Fig. 3

Fig. 5. Defect line resistance $\rho_{Wrinkle}$ for different wrinkles. For wrinkles #1 - #4 the colors indicate their position in Fig. 3a. Wrinkle #4 corresponds to that in Fig. 4. Gray line separates between unfolded (left) and folded graphene wrinkles (right). (A color version of this figure can be viewed online.)

as well as those from a similar map. All folded graphene wrinkles show a similar defect resistance; furthermore, standing wrinkles have comparable but slightly smaller defect resistances. We cannot exclude the presence of grain boundaries at these positions while it is likely to coincide, since the grain size in these samples is only of the order of several μm. On the other hand, since we did not observe any larger localized voltage drops in our sample, the line resistance of grain boundaries must be comparable to or smaller than 80 $\Omega\mu m$, which is again smaller than previous experimental reports [7,12].

We may understand the value of the folded wrinkle resistance if we note that the wrinkle can be modeled by two ML/TRL interfaces. As ML/BL-interfaces are known to have a defect resistance of 10–30 $\Omega\mu m$ [13,15], it is not surprising that a double ML/TRL interface might exhibit a value about twice as large. A more sophisticated model would have to take into account the particular structure of the defect: in case of no interlayer coupling, the defect resistance results simply from the additional path traveled by the electrons; this can be estimated, $\rho_{Wrinkle} = 2 \cdot \rho_{ML} \cdot L_{Wrinkle} \approx 200$ $\Omega\mu m$. This is not consistent with our observations. To accurately describe lower values of the defect resistance, interlayer tunneling has been proposed theoretically [11].

A folded wrinkle tunneling transport model is confirmed by our results, not only by the lower than expected value of the defect resistance through the folded wrinkle, but also by its temperature-independence. If the electron transport were simply governed by the elongated path, the defect resistance would increase due to the temperature-dependence of $\rho_{ML}(T)$. On the other hand, for tunneling between graphene sheets the resistance is lowered at elevated temperature due to thermal broadening of the Fermi distribution [28]. However, since this is a second order process the effect is rather small and not observable in our experiments. By modeling the interlayer tunneling process in a classical resistor network model (see Supporting Information) we can estimate the interlayer resistance to be $R_C \approx 8 \cdot 10^{-8} \Omega cm^2$ which we treated here as a contact resistance between two layers of graphene. This value is 2–3 orders of magnitudes larger than the bilayer interlayer resistance for graphene on SiC indicating a weaker coupling and a higher potential barrier [13]. Despite this, it is still smaller than, for example, the contact resistance between graphene and gold [20].

For the unfolded wrinkles (#1 and #2) the scattering mechanism must be a different because the path is almost not elongated and thus tunneling is not favored here. One possibility is the influence of grain boundaries as described above. An alternative explanation might invoke a scattering mechanism influenced by an induced potential by detachment of the graphene from the substrate as shown for steps for graphene on SiC [13,15,17]. For CVD-grown graphene, a local change in doping has been found at wrinkles and grain boundaries on the atomic scale by scanning tunneling spectroscopy [29,30].

3. Conclusion

In summary, we have utilized KPFM to map the spatial evolution of the electrostatic potential for CVD-grown graphene. By additional data processing we could disentangle the transport and electronic contribution to the mapped surface potential. We are able to quantify the local variations of the monolayer sheet resistance and to prove its local dependence on temperature. In contrast, local voltage drops across collapsed wrinkles gave only small contributions to the total resistance and did not depend on temperature. We suggest that this is due to a different scattering mechanism involving interlayer tunneling. All observed voltage drops reflected a line defect associated resistance <80 $\Omega\mu m$.

4. Methods

We used commercial graphene samples (Graphene Supermarket) on SiO_2 (285 nm) on p-doped Si-substrate with no additional gate voltage applied. While the KPFM measurements were done on one sample only, several samples where checked for similar morphology via normal AFM measurements. Since the samples showed no signs of contamination, no cleaning step was performed. Gold contacts were added in a shadow mask procedure and contacted by aluminum bond wires in a two-terminal geometry. Thus, we prepare large area graphene samples with a width $W = (520 \pm 20)$ μm and length $L = (260 \pm 20)$ μm.

KPFM is realized in a commercial setup (Agilent 5600LS). Atomic force and Kelvin force measurements are performed in tapping mode; amplitude modulation KPFM was used. For KPFM mode we used platinum deposited silicon cantilevers (OLYMPUS OMCL-AC240TM-B2) with a resonant frequency of 70 kHz and a spring constant 2 N/m.

The calibration of the sample temperature has been done by use of an infrared camera (Wöhler, EasIR-4). During the temperature measurements the same current densities and voltages as later in the KPFM experiments have been applied to the sample and subsequently, the temperature was mapped in the middle of the graphene sample. This yield a quadratic relation $T = (0.0089 \pm 0.0002) \frac{m^2}{A^2} K \cdot j_{macro}^2 + (298.9 \pm 0.7) K$ as expected for Joule-heating. While the temperature might not be homogeneous about the sample, e.g. at the contacts, the KPFM maps were taken in the middle where also the temperature was measured. Due to the high homogeneity in current density, we assumed Joule heating and thus the temperature to be constant on the ML graphene sheets.

Measurements have been taken over several days and with different tips, especially the data shown in Fig. 4 demonstrate their reproducibility.

For the evaluation of the local voltage drops, all lines of a map have been shifted along the x-direction to give a straight line as depicted in Fig. 4b. Thus, averaging along the y-axis improves the statistics and thus the resolution of the voltage drop. This method is valid for a small voltage drop in y-direction which we demonstrated in Fig. 2g. For inclined wrinkles a correction factor of $cos\theta$ has been introduced corresponding to the projection in the direction of the current in order to reproduce the actual voltage drop.

Author Contributions

M.W., P.W., A.W. and H.Y. planned the experiments. P.W., A.S., C.M. performed the AFM measurements. T.K. and P.W. performed the resistor network simulations. The manuscript was written through contributions of all authors. All authors have given approval to the final version of the manuscript.

Acknowledgment

Appendix A. Supplementary data

Supplementary data related to this article can be found at http://dx.doi.org/10.1016/j.carbon.2016.02.067.

References

[1] A.K. Geim, K.S. Novoselov, The rise of graphene, Nat. Mater. 6 (2007) 183—191, http://dx.doi.org/10.1038/nmat1849.

[2] D. Akinwande, N. Petrone, J. Hone, Two-dimensional flexible nanoelectronics, Nat. Commun. 5 (2014) 5678, http://dx.doi.org/10.1038/ncomms6678.

[3] H.K. Yu, K. Balasubramanian, K. Kim, J.L. Lee, M. Maiti, C. Ropers, et al., Chemical vapor deposition of graphene on a "Peeled-off" epitaxial Cu (111) foil: a simple approach to improved properties, ACS Nano 8 (2014) 8636—8643, http://dx.doi.org/10.1021/nn503476j.

[4] X. Li, W. Cai, J. An, S. Kim, J. Nah, D. Yang, et al., Large-area synthesis of high-quality and uniform graphene Films on copper foils, Science 324 (2009) 1312—1314, http://dx.doi.org/10.1126/science.1171245.

[5] J.H. Lee, E.K. Lee, W.J. Joo, Y. Jang, B.S. Kim, J.Y. Lim, et al., Wafer-scale growth of single-crystal monolayer graphene on reusable hydrogen-terminated germanium, Science 344 (2014) 286—289, http://dx.doi.org/10.1126/science.1252268.

[6] P.Y. Huang, C.S. Ruiz-Vargas, A.M. van der Zande, W.S. Whitney, M.P. Levendorf, J.W. Kevek, et al., Grains and grain boundaries in single-layer graphene atomic patchwork quilts, Nature 469 (2010) 389—392, http://dx.doi.org/10.1038/nature09718.

[7] K.W. Clark, X.G. Zhang, I.V. Vlassiouk, G. He, R.M. Feenstra, A.P. Li, Spatially resolved mapping of electrical conductivity across individual domain (grain) boundaries in graphene, ACS Nano 7 (2013) 7956—7966, http://dx.doi.org/10.1021/nn403056k.

[8] A.W. Tsen, L. Brown, M.P. Levendorf, F. Ghahari, P.Y. Huang, R.W. Havener, et al., Tailoring electrical transport across grain boundaries in polycrystalline graphene, Science 336 (2012) 1143—1146, http://dx.doi.org/10.1126/science.1218948.

[9] Q. Yu, L.A. Jauregui, W. Wu, R. Colby, J. Tian, Z. Su, et al., Control and characterization of individual grains and grain boundaries in graphene grown by chemical vapour deposition, Nat. Mater. 10 (2011) 443—449, http://dx.doi.org/10.1038/nmat3010.

[10] D.L. Duong, G.H. Han, S.M. Lee, F. Gunes, E.S. Kim, S.T. Kim, et al., Probing graphene grain boundaries with optical microscopy, Nature 490 (2012) 235—239, http://dx.doi.org/10.1038/nature11562.

[11] W. Zhu, T. Low, V. Perebeinos, A.A. Bol, Y. Zhu, H. Yan, et al., Structure and electronic transport in graphene wrinkles, Nano Lett. 12 (2012) 3431—3436, http://dx.doi.org/10.1021/nl300563h.

[12] K.L. Grosse, V.E. Dorgan, D. Estrada, J.D. Wood, I. Vlassiouk, G. Eres, et al., Direct observation of resistive heating at graphene wrinkles and grain boundaries, Appl. Phys. Lett. 105 (2014) 143109, http://dx.doi.org/10.1063/1.4896676.

[13] P. Willke, T. Druga, R.G. Ulbrich, M.A. Schneider, M. Wenderoth, Spatial extent of a Landauer residual-resistivity dipole in graphene quantified by scanning tunnelling potentiometry, Nat. Commun. 6 (2015) 6399, http://dx.doi.org/10.1038/ncomms7399.

[14] W. Wang, K. Munakata, M. Rozler, M.R. Beasley, Local transport measurements at mesoscopic length scales using scanning tunneling potentiometry, Phys. Rev. Lett. 110 (2013) 236802, http://dx.doi.org/10.1103/PhysRevLett.110.236802.

[15] S.-H. Ji, J.B. Hannon, R.M. Tromp, V. Perebeinos, J. Tersoff, F.M. Ross, Atomic-scale transport in epitaxial graphene, Nat. Mater. 11 (2012) 114—119, http://dx.doi.org/10.1038/nmat3170.

[16] K.H. Bevan, A first principles scanning tunneling potentiometry study of an opaque graphene grain boundary in the ballistic transport regime, Nanotechnology 25 (2014) 415701, http://dx.doi.org/10.1088/0957-4484/25/41/415701.

[17] T. Low, V. Perebeinos, J. Tersoff, P. Avouris, Deformation and Scattering in Graphene over Substrate Steps, Phys. Rev. Lett. 108 (2012) 096601, http://dx.doi.org/10.1103/PhysRevLett.108.096601.

[18] J.H. Chen, C. Jang, S. Xiao, M. Ishigami, M.S. Fuhrer, Intrinsic and extrinsic performance limits of graphene devices on SiO2, Nat. Nanotechnol. 3 (2008) 206—209.

[19] P. Willke, J.A. Amani, A. Sinterhauf, S. Thakur, T. Kotzott, T. Druga, et al., Doping of graphene by low-energy ion beam implantation: structural, electronic and transport properties, Nano Lett. 15 (2015) 5110—5115, http://dx.doi.org/10.1021/acs.nanolett.5b01280.

[20] T. Druga, M. Wenderoth, F. Lüpke, R.G. Ulbrich, Graphene-metal contact resistivity on semi-insulating 6H-SiC (0001) measured with Kelvin probe force microscopy, Appl. Phys. Lett. 103 (2013) 051601, http://dx.doi.org/10.1063/1.4816955.

[21] Y.J. Yu, Y. Zhao, S. Ryu, L.E. Brus, K.S. Kim, P. Kim, Tuning the graphene work function by electric field effect, Nano Lett. 9 (2009) 3430—3434, http://dx.doi.org/10.1021/nl901572a.

[22] V. Panchal, R. Pearce, R. Yakimova, A. Tzalenchuk, O. Kazakova, Standardization of surface potential measurements of graphene domains, Sci. Rep. 3 (2013) 2597, http://dx.doi.org/10.1038/srep02597.

[23] L. Yan, C. Punckt, I.A. Aksay, W. Mertin, G. Bacher, Local voltage drop in a single functionalized graphene sheet characterized by Kelvin probe force microscopy, Nano Lett. 11 (2011) 3543—3549, http://dx.doi.org/10.1021/nl201070c.

[24] S. Ladak, J.M. Ball, D. Moseley, G. Eda, W.R. Branford, M. Chhowalla, et al., Observation of wrinkle induced potential drops in biased chemically derived graphene thin film networks, Carbon 64 (2013) 35—44, http://dx.doi.org/10.1016/j.carbon.2013.06.051.

[25] D. Pan, E. Fuller, O.T. Gul, P.G. Collins, One-dimensional Poole-Frenkel conduction in the single defect limit, Nano Lett. 15 (2015) 5248—5253, http://dx.doi.org/10.1021/acs.nanolett.5b01506.

[26] Y. Zhang, Q. Chen, A.P. Alivisatos, M. Salmeron, Dynamic charge carrier trapping in quantum dot field effect transistors, Nano Lett. 15 (2015) 4657–4663, http://dx.doi.org/10.1021/acs.nanolett.5b01429.

[27] D. Ziegler, P. Gava, J. Güttinger, F. Molitor, L. Wirtz, M. Lazzeri, et al., Variations in the work function of doped single-and few-layer graphene assessed by Kelvin probe force microscopy and density functional theory, Phys. Rev. B 83 (2011) 235434, http://dx.doi.org/10.1103/PhysRevB.83.235434.

[28] C. Uher, R.L. Hockey, E. Ben-Jacob, Pressure dependence of the c-axis resistivity of graphite, Phys. Rev. B 35 (1987) 4483, http://dx.doi.org/10.1103/PhysRevB.35.4483.

[29] J.C. Koepke, J.D. Wood, D. Estrada, Z.-Y. Ong, K.T. He, E. Pop, et al., Atomic-scale evidence for potential barriers and strong carrier scattering at graphene grain boundaries: a scanning tunneling microscopy study, ACS Nano 7 (2012) 75–86, http://dx.doi.org/10.1021/nn302064p.

[30] L. Tapasztó, P. Nemes-Incze, G. Dobrik, K.J. Yoo, C. Hwang, L.P. Biró, Mapping the electronic properties of individual graphene grain boundaries, Appl. Phys. Lett. 100 (2012) 053114, http://dx.doi.org/10.1063/1.3681375.